Hydraulic Fracture Propagation and Proppant Transport Mechanism in Interlayered Reservoir

Jue Wang [1,*], Genbo Peng [2], Ziyuan Cong [2] and Buqin Hu [2]

1   Department of Petroleum Engineering, Northeast Petroleum University, Daqing 163318, China
2   School of Environment, Liaoning University, Shenyang 110036, China
*   Correspondence: wangjue@nepu.edu.cn

Abstract: Hydraulic fracture is crucial for assuring well production from unconventional reservoirs. For the optimization of hydraulic fracture geometry and the ensuing production of an interlayered reservoir, vertical hydraulic fracture propagation path has been analyzed. However, an effective fluid channel cannot be formed if the proppant is unable to reach the area where the fracture propagates. This paper presents a numerical model using the lattice-based method to investigate the hydraulic fracture propagation and proppant transport mechanism in interlayered reservoirs. The hydraulic fracture propagation model was simulated under different geological and fracturing engineering factors. The results indicate that interlayer Young's modulus and horizontal stress anisotropy are positively correlated with longitudinal propagation and proppant carrying ability in interlayered formations. The fracturing injection rate has an optimal solution for fracture propagation and proppant carrying since a too low injection rate is unfavorable for fracture penetration of the interlayer, while a too high injection rate increases fracture width instead of further fracture penetration. In conclusion, attention is drawn to fine particle size proppants used in multi-layer reservoirs for fracturing fluid to carry proppants as far as possible to obtain maximum propped area.

Keywords: interlayered reservoir; vertical propagation; proppant transport; lattice-based method

1. Introduction

Shale oil resources, with their wide distribution and enormous exploitation potential, play a critical role in achieving China's energy strategy and meeting its energy demand. There are primarily two types of formations based on lithological structures: pure shale and shale interlayered formation. Multiple pay layers are separated by interlayers with varying thickness in the vertical orientation, which is incapable of hydrocarbon migration and production [1–5]. In order to improve economic productivity, horizontal well and combined-layer-penetration fracturing are proposed. Hydraulic fracturing (HF) is a widely used production enhancement technique that increases permeability to improve well production performance by injecting high-pressure fluid into the reservoir to create a fluid channel [6–12]. Hydraulic fracture propagation enables multiple layers to be connected with a single operation. Therefore, those fractures formed by fracturing are used as flow channels to produce oil and gas from adjacent multiple pay layers near the wellbore.

Proppant is a small solid particle mixed with the fracturing fluid and pumped into the fracture to prop it up and prevent it from closing [13–16]. Due to the high cost of fracturing operations, accurate predictions of the fracture morphology after fracturing are required to ensure maximum operational effectiveness. However, in interlayered formations, differences in formation parameters, such as stress anisotropy and rock lithology between layers, results in complex morphological changes in the fracture during propagation. This poses a challenge for fracture morphology prediction.

Previous studies have focused on planar fracture propagation, mainly investigating fracture length and width [17–21], and have made many breakthroughs in accurately

predicting the fracture morphology under different in situ stresses, rock properties, and fracturing parameters. However, relatively few studies have been conducted to address the propagation of fractures at height in multi-layer reservoirs, which is attributed to the significant differences in rock properties and stresses in the vertical direction between layers. For this reason, researchers have proposed several computational methods to study the fracture propagation behavior in the vertical direction [22–25]. Simonson et al. [26] developed a fracture height growth model for three symmetric formations. Ahmed [27], Newberry, et al. [28], Economides [29], and others modified Simonson's model. Li et al. [30] developed and solved a mathematical model of hydraulic fracture height for highly stressed multilayered complex formations based on the effect of a plastic zone on fracture height growth (generated by stress concentration at the fracture tip), and systematically described the effects of rock stress, fracture toughness, fracture fluid density, and other factors on fracture height growth. The above research has laid a solid foundation for studying the mechanism of high fracture growth in unconventional reservoirs. However, based on extensive field tests, proppant only accounts for a small fraction of the fracture [31–35]. The fracture height formed by fracturing is not equal to the height of the final fluid channel that can be obtained; the degree of proppant filling over the fracture height determines the final fracture height.

Therefore, the success of hydraulic fracturing treatments requires the formation of a proppant-filled conductive channel connecting the created fracture zone to the wellbore. The goal of fracturing is to maximize the area of the pay zone connected to the wellbore by a propped channel. However, the placement of the proppant in the hydraulic fracture is a complex process. Much effort has been devoted to modeling this behavior because a thorough understanding of the proppant transport in the opened fracture is crucial to optimize the hydraulic fracture design, which in turn improves the unconventional well production performance. Proppant transport is related to its type, shape, concentration, and density. These properties affect the suspension and transport of proppant in the fracturing fluid and play a decisive role in the final settlement location of proppant, which in turn affects the fracture conductivity.

Keshavarz et al. [36] analyzed the size effect of proppant in stimulating naturally fractured coalbed methane (CBM) formations. The authors developed a laboratory-based mathematical model to simulate the transport process. The results were validated in comparison with the model created by Khanna et al. [37]. They observed that the injection of micro-sized proppant particles kept the natural fractures open and increased the fractured reservoir volume (SRV) and production capacity. The micro-sized proppant also reduced the leakoff into the natural fractures during hydraulic fracturing. This provides insight into the proppant size effect on the propping effect during the fracturing of an interlayered reservoir.

Most studies have focused on the mechanism of vertical fracture propagation and the final fracture morphology. However, the fractures formed during the fracturing process need proppant support after the fracturing is completed to form fluid channels but the proppant often cannot fully prop fractures. Therefore, it is necessary to investigate the settlement and the propping effect of proppant in the fracture after the fracture is grown vertically through the layer surface into the interlayer. This paper is organized as follows: In Section 2, we present the simulation method of the problem, and discuss the mechanical model, flow model, flow mechanical coupling, and proppant transport of the XSite simulator. In Section 3, we briefly present the model setting of cases simulated in this paper. In Section 4, we do a sensitivity analysis considering the effect of Young's modulus, stress anisotropy, and fluid injection rate on the proppant transport, while Sections 5 and 6 discuss the findings of this work.

2. Simulation Method

The XSite lattice simulator, which was based on discrete element method (DEM) used in this study for simulation purposes, was developed by the Itasca Consulting Group with

the application of synthetic rock mass (SRM) [38]. It is able to simulate the interaction between the HF and natural interface (NI) without predefining propagation path and mechanism of interaction. The smooth joint model (SJM) represents the pre-existing joints in the simulator while the lattice simulates the propagation of the fracture in the rock.

2.1. Mechanical Model

Lattice nodes linked by normal and shear springs are randomly placed in the simulator to simulate the rock mass. To simulate the translational motion of each node, the following central difference formulas of linear momentum equilibrium and displacement-velocity relation are employed [38].

$$\dot{u}_i^{(t+\Delta t/2)} = \dot{u}_i^{(t-\Delta t/2)} + \sum F_i^{(t)} \Delta t / m \tag{1}$$

$$u_i^{(t+\Delta t)} = u_i^{(t)} + \dot{u}_i^{(t+\Delta t/2)} \Delta t \tag{2}$$

where $\dot{u}_i^{(t)}$ and $u_i^{(t)}$ represent the velocity and position of component i ($I = 1, 3$) at time t, and $\sum F_i$ represents the sum of all force components acting on mass m at the time step of Δt. Likewise, the angular velocities, ω_i, of component can be obtained as:

$$\omega_i^{(t+\Delta t/2)} = \omega_i^{(t-\Delta t/2)} + \frac{\sum M_i^{(t)}}{I} \Delta t \tag{3}$$

where $\sum M_i$ represents the sum of all moment components acting on the moment of inertia I node. The relative displacement and spring force variations are determined by the node velocities:

$$F^N \leftarrow F^N + \dot{u}^N k^N \Delta t \tag{4}$$

$$F_i^S \leftarrow F_i^S + \dot{u}_i^S k^S \Delta t \tag{5}$$

where "N" denotes "Normal" and "S" denotes "shear"; k^N and k^S represent the spring normal and shear stiffnesses, respectively.

The following equations indicate the relevant correlations between the micro spring and the macro rock mass in terms of tensile strength and shear strength:

$$F^{Nmax} = \alpha_t T R^2 \tag{6}$$

$$F^{Nmax} = \mu F^{Nmax} + \alpha_s C R^2 \tag{7}$$

where F^{Nmax} represents the spring tensile strength and F^{Smax} represents the spring shear strength; α_t and α_s represent the calibration coefficient of tensile and shear strength, respectively. T represents tensile strength of macro rock mass, μ represents the friction coefficient, C represents the shear strength of macro rock, and R represents the resolution.

2.2. Flow Model

Fluid flow is simulated within both the intact rock matrix and the joints. Within the network of fluid nodes connected by the pipe, the flow in the fractures can be resolved. Meanwhile, the flow leakoff into the intact rock is considered matrix flow and depends on the permeability of the intact rock. The flow in a fracture may be roughly estimated using the lubrication equation. This flow down the pipe from node "A" to node "B" can be calculated as [38]:

$$q = \beta k_r \frac{a^3}{12\mu_f} \left[P^A - P^B + \rho_w g \left(Z^A - Z^B \right) \right] \tag{8}$$

Here, a is hydraulic aperture, μ_f is viscosity of the fluid, and P^A and P^B represent fluid pressures at node "A" and "B", respectively. Z is elevations of nodes, ρ_w represents fluid density, and g represents the acceleration due to gravity. Meanwhile, k_r represents the relative permeability and β represents a dimensionless calibrated parameter, which is a calibrated function of model resolution [38].

2.3. Hydro-Mechanical Coupling

In XSite, hydraulic fracture propagation is represented by processes that are mechanical and fluid flow coupling. The fracture aperture and the deformation mechanism of the model regulate the permeability of the fracture. Based on the change in fluid pressure, the deformation and damage of the mechanical model are calculated. Conversely, the fluid pressure varies with the deformation [38]. The hydro-mechanical coupling included in the models is shown here is as follows.

1. Aperture or the deformation of the solid model determines the fracture permeability.
2. Fluid pressure has an impact on both the deformation and the strength of the solid model. Calculations of the effective stress are performed.
3. The fluid pressures are impacted by the deformation of the solid model. In particular, the code can predict changes in fluid pressure under undrained conditions.

2.4. Proppant Transport and Placement

It is mentioned that all flow paths are formulated as one-dimensional pipes due to advection and splitting; this conforms to the following advection equation.

$$\frac{\partial C}{\partial t} = -v\frac{\partial C}{\partial x} \tag{9}$$

where C represents the proppant concentration, kg/m^3; v represents the fluid velocity, m/s.

Due to the constant mass of the proppant, the proppant concentration is also updated when the fracture aperture changes. The new concentration may be determined using the change in volume (from V_i to j V_{i+1}) of the node.

$$C_{i+1} = C_i\frac{V_i}{V_{i+1}} \tag{10}$$

where C_i and C_{i+1} represent the proppant concentration before and after the step, kg/m^3, respectively. The ratio between concentration and the initial unload density of proppant is the criterion for proppant taking load.

$$R = \frac{\rho_u}{C} \tag{11}$$

where ρ_u represents the initial density of proppant, kg/m^3.

If $R < 1$, the proppant loaded; otherwise, it is not loaded. When the proppant is loaded, the mechanical impact of proppant on the normal force can be expressed as:

$$\Delta F_n = -\frac{(\Delta P + \Delta\sigma)Ak_n}{k_n + k_J} \tag{12}$$

where $\Delta\sigma$ represents the change in proppant stress, N; A represents the apparent area of the joint element, m^2; k_n is the rock stiffness, N/m; k_J is the joint normal stiffness, N/m.

Borehole segments are natural equivalents to pipes and the flow in a 2D fracture is idealized by a network of pipes in the plane of the fracture. Therefore, the proppant model function of this simulator is fully suitable for simulating hydraulic fracturing proppant carry ability to study in the interlayered formation.

3. Model Setting

　　Based on actual geological conditions, a model as depicted in Figure 1 was established. The model measures $8 \times 8 \times 8$ m^3 and consists of five layers. The middle layer comprises a 2 m-thick pay layer with a horizontal well placed within it; a fracture is located at the center of this well for the hydraulic fracture initiation. The pay layer is flanked by two 1 m-thick interlayers on either side; a cemented fracture characterizes the interface between these interlayers and the pay layer. In this model, the maximum, minimum, and vertical principal stresses are oriented along the X, Y, and Z directions, respectively. Table 1 exhibits all rock mechanical properties and fracturing fluid injection parameters for the model; all mechanical properties parameters were obtained from laboratory mechanical tests.
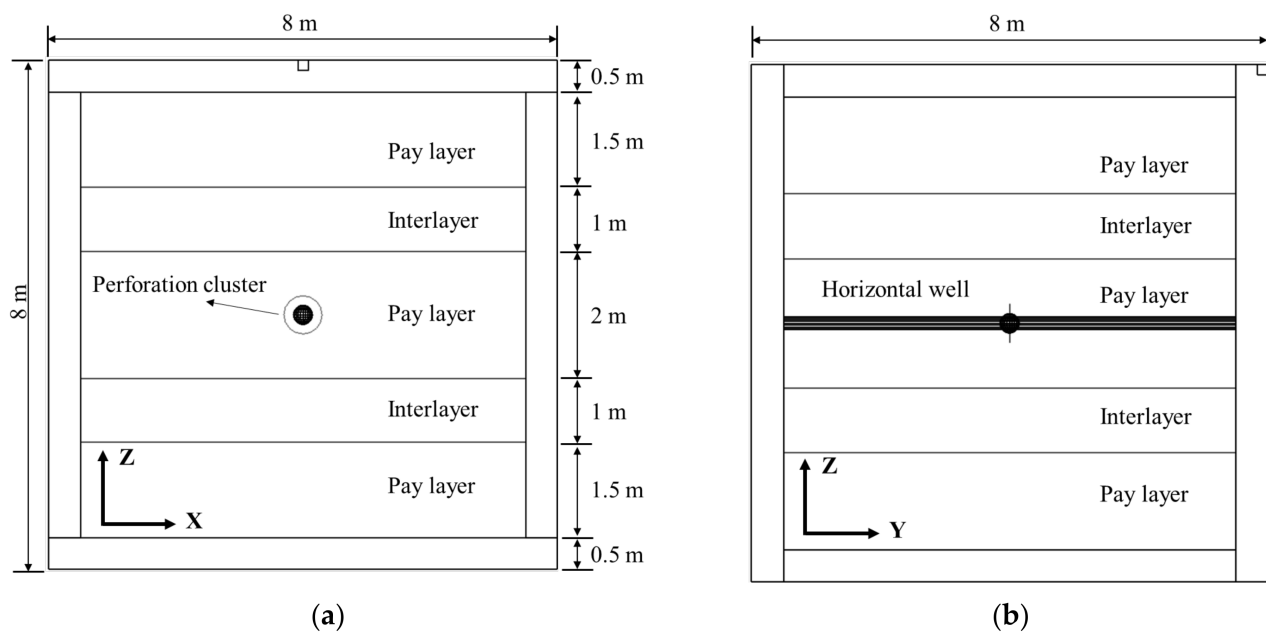
Figure 1. Hydraulic fracture propagation numerical model of the interlayered reservoir: (**a**) Front view of the model. (**b**) Left view of the model.

Table 1. Rock mechanical parameters and fracturing fluid pumping parameters used for the simulation study.

Parameters	Pay Layer
Tensile strength (MPa)	3.5
Uniaxial compressive strength (MPa)	79.5
Young's modulus (GPa)	27.7
Poisson's ratio	0.221
Permeability (10^{-15} m^2)	1.7
Vertical in situ stress (MPa)	10
Minimum horizontal principal stress (MPa)	5
Maximum horizontal principal stress (MPa)	8
Pumping rate of fracturing fluid (m^3/s)	0.06
Viscosity of fracturing fluid (Pa·s)	0.001

　　Small particle size quartz sand has dominated the proppant industry in North America. In fact, the sum of 40/70 mesh and 100 mesh fine sands used in the shale gas industry in North America accounted for more than 70% of the total proppant used in 2018 [39,40]

(Figure 2). Moreover, 40/70 mesh and 100 mesh fine sands exceeded 80% in the first quarter of 2019, and even 100 mesh quartz sand in deeper layers at depths of 3500 m exceeded 68.6% [41–43]. Therefore, based on the proportion of proppant of each grain size in Figure 2, this study selected relatively course 42 mesh, and the fine 80 and 100 mesh proppants to investigate their effect on the fracture propped area at various grain sizes.
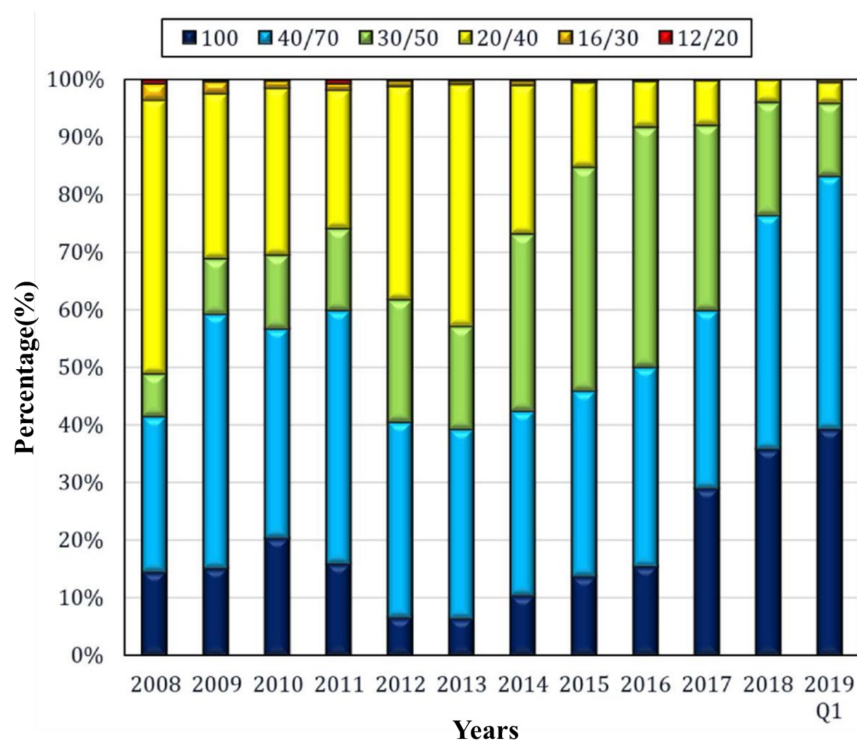

**Figure 2.** Shale gas proppant size distribution in North America, 2008–2019.

4. Results

This section investigates the effects of reservoir mechanical and operational parameters on fracture propagation and proppant distribution in the fracturing fluid during fracturing using a numerical model of fracture propagation in multi-layer reservoirs.

4.1. Effect of Young's Modulus

Some studies have concluded that mechanical parameters with low Young's modulus favor fracture propagation, while high Young's modulus is detrimental to fracture propagation. However, some field observations found that low Young's modulus did not promote fracture propagation as expected. To clarify the effect of Young's modulus on fracture propagation, this section assumed a constant pay layer Young's modulus of 27.7 GPa and interlayer Young's modulus of 10, 15, 20, 27.7, and 40 GPa to carry out a study of the effect of interlayer Young's modulus on fracture propagation in the height direction and proppant distribution, as shown in Figure 3. When Young's modulus of the interlayer is 10 GPa, the fracture cannot penetrate the upper and lower interlayer, and can only propagate in the pay layer. When Young's modulus of the interlayer is 15 GPa, the fracture enables the interlayer to be penetrated after initiation in the pay layer; due to the heterogeneity of the reservoir, the fracture fails to penetrate the upper and lower interlayer synchronously to form a symmetric fracture, and only carries proppants penetrating the upper interlayer. When Young's modulus is 20 GPa, the fracture penetrates the upper and lower interlayer synchronously to form a relatively symmetric fracture. When Young's modulus of the interlayer is 27.7 GPa, i.e., the pay layer and the interlayer have the same Young's modulus, the fracture morphology formed by fracturing shows a relatively perfect circle and is not

affected by the layer interface, and, when Young's modulus of the interlayer is 40 GPa, it also has a similar fracture morphology.
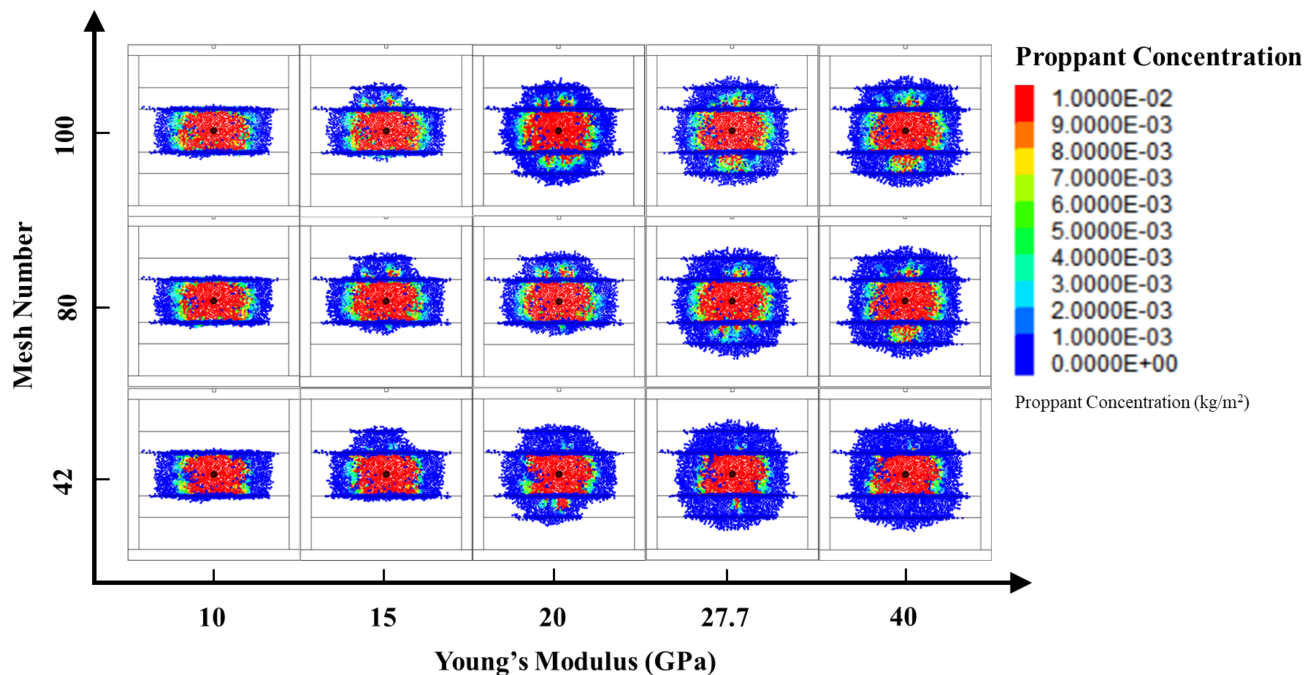
Figure 3. Variation of hydraulic fracture vertical propagation stimulated and propped area with interlayer Young's modulus.

From Figure 4, it can be found that, with an increase in Young's modulus, the fracturing stimulated area continuously increases, showing a low Young's modulus inhibits fracture propagation and a high Young's modulus promotes fracture propagation. This is consistent with the findings of previous studies [44,45]: a large elastic modulus promotes fracture height growth and inhibits fracture width.

From Figure 5, it can be found that, with an increase in Young's modulus, the propped area generally shows an increasing trend but, when the proppant particle size is 42 mesh, the maximum propped area appears when Young's modulus is 20 GPa. This is because with the increase in Young's modulus in the interlayer, even though the propagation area of the fracture increases, the high Young's modulus in the interlayer makes the width of the formed fracture relatively low, which is not conducive to the inflow of proppant. In contrast, when the proppant particle size is 80 or 100 mesh, the propped area formed under the same formation conditions increases significantly due to the reduction in proppant particle size. Moreover, the propped area generally shows a monotonic increase with the increase in Young's modulus.

The propped area ratio is defined as the ratio of the propped area to the total fracturing stimulated area in the fracture height direction. From Figure 6, it can be found that the propped area ratio slowly decreases with the increase in Young's modulus. In essence, when Young's modulus is 10 GPa, the hydraulic fracture fails to penetrate the interface; thus, the propped area ratio is the ratio of the propped area to the total fracture area in the reservoir. However, when Young's modulus is 15 GPa and 20 GPa, partial hydraulic fractures enable the interface to penetrate into the interlayer and, considering the inhibiting effect of the interlayer on the proppant transport into the interlayer, the propped area in the interlayer is relatively small, which ultimately reduces the overall propped area ratio. When Young's modulus is 27.7 GPa and 40 GPa, the greatly increased fracture area and the slightly increased propped area result in a further decrease in the propped area ratio.

In conclusion, Young's modulus has an inhibiting effect on the propped area ratio, essentially because, as the Young's modulus of the interlayer increases, even though the

fracture enables the upper and lower interlayer to be penetrated to significantly increase the fracture area, only a small amount of proppant enters the interlayer resulting in an insignificant increase in the propped area, making the overall trend of the propped area ratio decrease. In addition, the difference in particle size also has a non-negligible effect on the propped area ratio of fractures in multi-layer reservoirs. Under the same conditions, the propped area ratio of a relatively large particle size proppant is smaller than that of a small one and the difference in the amount of proppant entering the interlayer to play a propping role due to the difference in particle size is essential for this phenomenon.
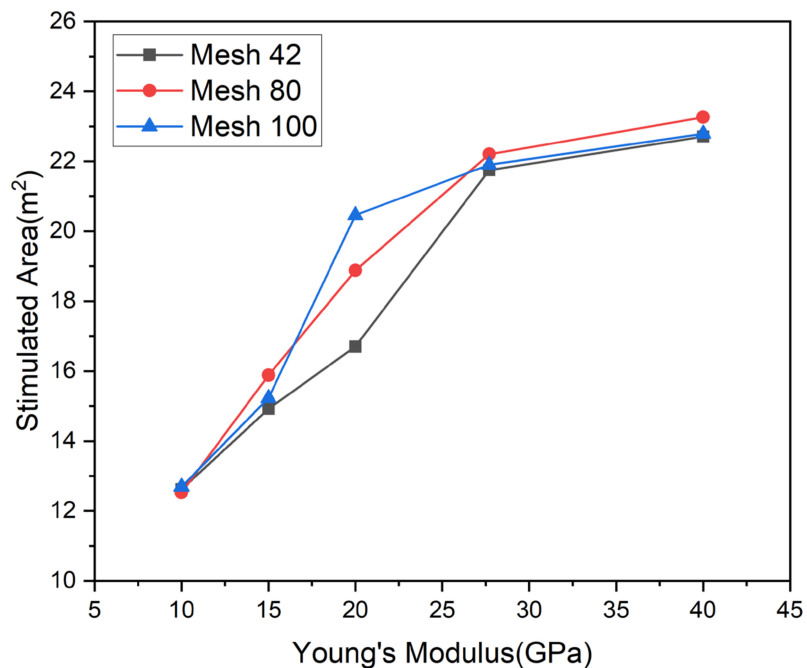

Figure 4. Effect of interlayer Young's modulus on fracture stimulated area.
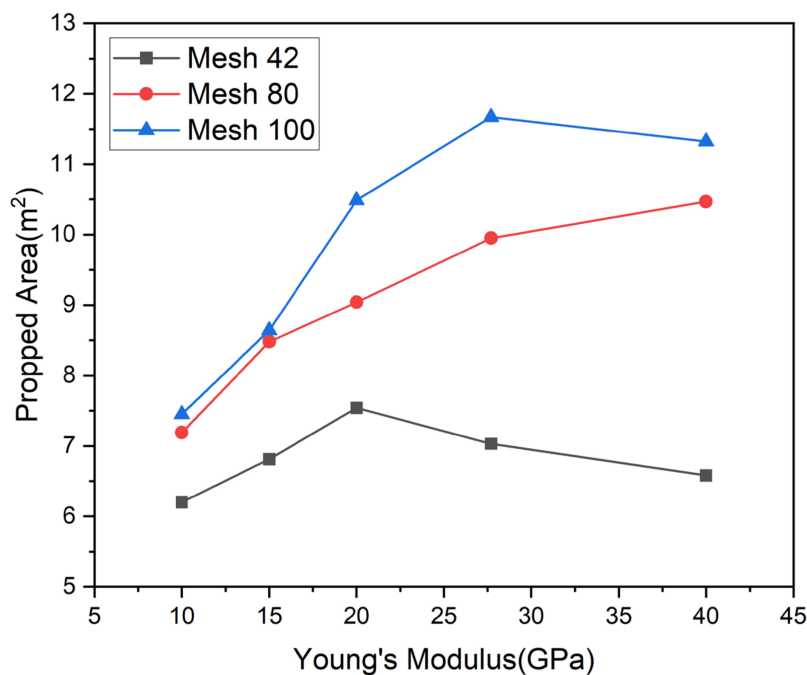

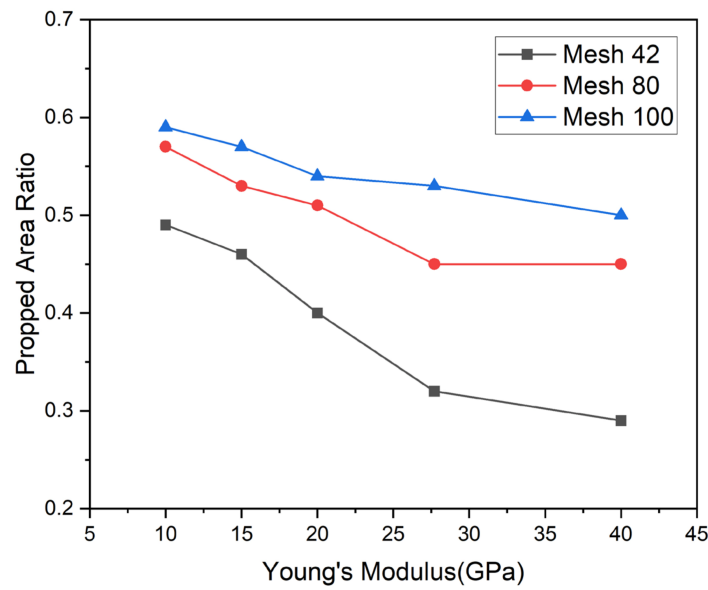**Figure 5.** Effect of interlayer Young's modulus on propped area.

Figure 6. Effect of interlayer Young's modulus on propped area ratio.

4.2. Effect of Stress Anisotropy

In this section, we obtain different horizontal stress anisotropy by varying the minimum principal stress to study the effect of stress anisotropy on fracture morphology and proppant transport. Maintaining the maximum principal stress constant at 8 MPa, the minimum principal stress was set to 7, 6, 5, 4, and 3 MPa to obtain horizontal stress anisotropy of 1, 2, 3, 4, and 5 MPa, and the fracture morphology is shown in Figure 7. When the stress anisotropy is 1 MPa, the fracture growth in the upper and lower direction is inhibited and can only propagate in the pay layer. When the stress anisotropy is 2 MPa, though the main body of the fracture propagates in the pay layer, the fracture can penetrate the upper and lower interlayers locally. When the stress anisotropy reaches 3 MPa, the fracture extends into a penny shape fracture, which can evenly penetrate the upper and lower interlayer, ensuring the symmetrical fracture morphology up and down. Increasing the stress anisotropy only slightly affects the total fracturing stimulated area but does not affect its shape.
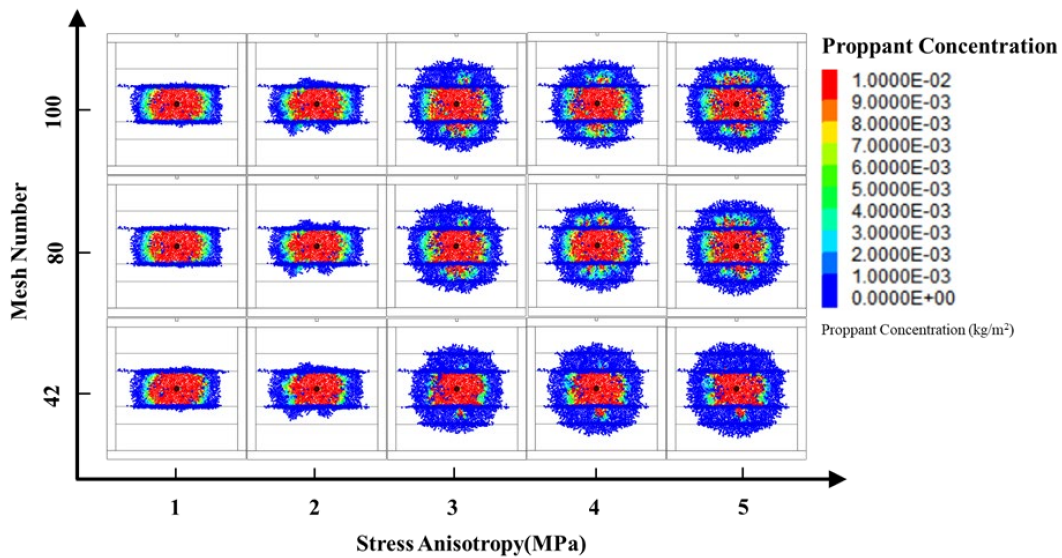

Figure 7. Variation of hydraulic fracture vertical propagation stimulated and propped area with stress anisotropy.

From Figure 8, it can be seen that the fracturing stimulated area gradually increases with the increase in stress anisotropy. When the stress anisotropy increases from 2 mPa to 3 mPa, the maximum increase in a stimulated area increases by nearly 7 m^2. Combining with Figure 7, it can be found that the increase in stimulated area is due to the fracture penetrating the layer interface into the upper and lower interlayer, which is attributed to the high-pressure fluid inside the fracture caused by the high stress anisotropy, making the fracture gain more energy for penetrating the interlayer, thus substantially increasing the stimulated area.
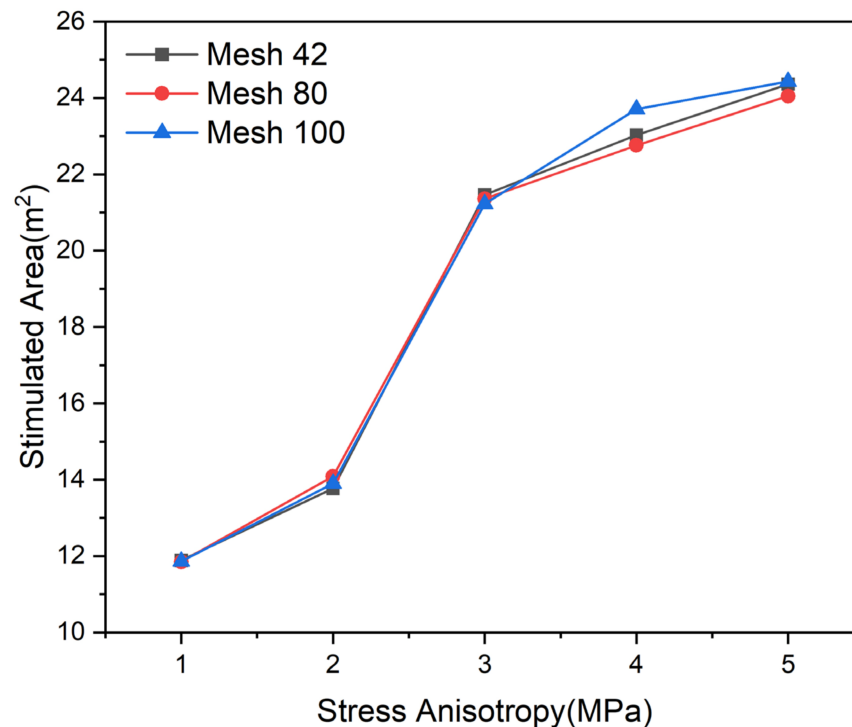
Figure 8. Effect of stress anisotropy on fracture stimulated area.

From Figure 9, it can be seen that the propped area shows an overall increasing trend with the stress anisotropy. However, different proppant particle sizes have a varying influence on the propping effect. Typical is the propping effect gap between coarse particle sizes 42 mesh, and fine particle sizes 80 and 100 mesh. When the particle size is 42 mesh, even though the pressurized fluid enters the interlayer under high stress anisotropy, it is more difficult for the coarse particle size proppant transport into the interlayer to form an effective propping. In contrast, the 80 and 100 mesh particle size proppant entered the interlayer relatively easily and formed effective propping for the fractures in the interlayer.
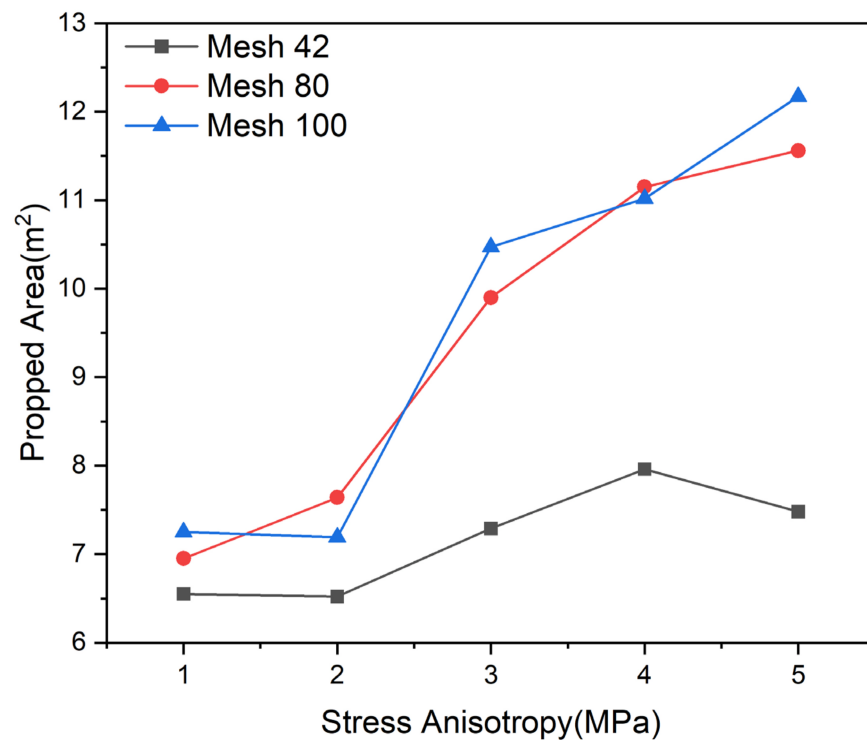
Figure 9. Effect of stress anisotropy on the propped area.

As shown in Figure 10, the overall propped area ratio decreases with increasing stress anisotropy. Similarly, the overall propped area ratio of 42 mesh proppant with coarse particle size is lower than that of 80 and 100 mesh. This is because with the close stimulated area, the coarser particle size can prop less area, thus reducing the overall propped area ratio.
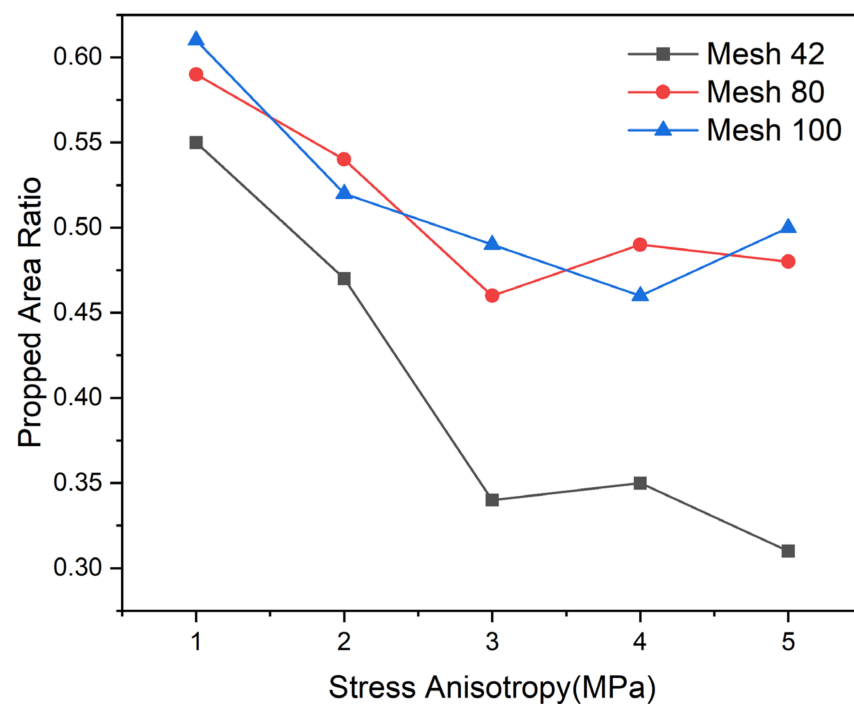

Figure 10. Effect of stress anisotropy on propped area ratio.

In conclusion, the greater the stress anisotropy is, the larger the fracture area is, and the propped area also increases along with the fracture penetrating into the interlayer. Also, due to the inconsistent rate of these two kinds of area increase, the propped area ratio decreases.

4.3. Effect of Injection Rate

The fracturing fluid injection rate is one of the most controllable operational parameters. Reasonable control of the injection rate not only creates a fracture morphology that maximizes production but also provides significant operation cost savings. The injection rate affects the post-fracturing fracture morphology by influencing the pressure of the fluid during the fracturing process.

As shown in Figure 11, the fracturing fluid injection rate is increased from 0.01 to 0.06 m^3/s to analyze the effect of injection rate on fracture morphology. Here, the rock mechanical properties of the interlayer are kept consistent with the pay layer and only the effect of fracturing fluid injection rate is considered. When the injection rate is 0.01 m^3/s, the fracture propagates only in the middle pay layer. When the injection rate increases to 0.02 m^3/s, the fracture penetrates downward into the lower interlayer, whereas it fails to penetrate the upper interlayer, forming a symmetric fracture morphology. This type of asymmetric fracture propagation often occurs during actual fracturing because of the heterogeneity in varying layers. When the injection rate increases to 0.04 m^3/s, the fractures penetrate the upper and lower interlayer synchronously, the fracture morphology is close to the penny shape, and the layer interface has negligible inhibition of the fracture propagation.
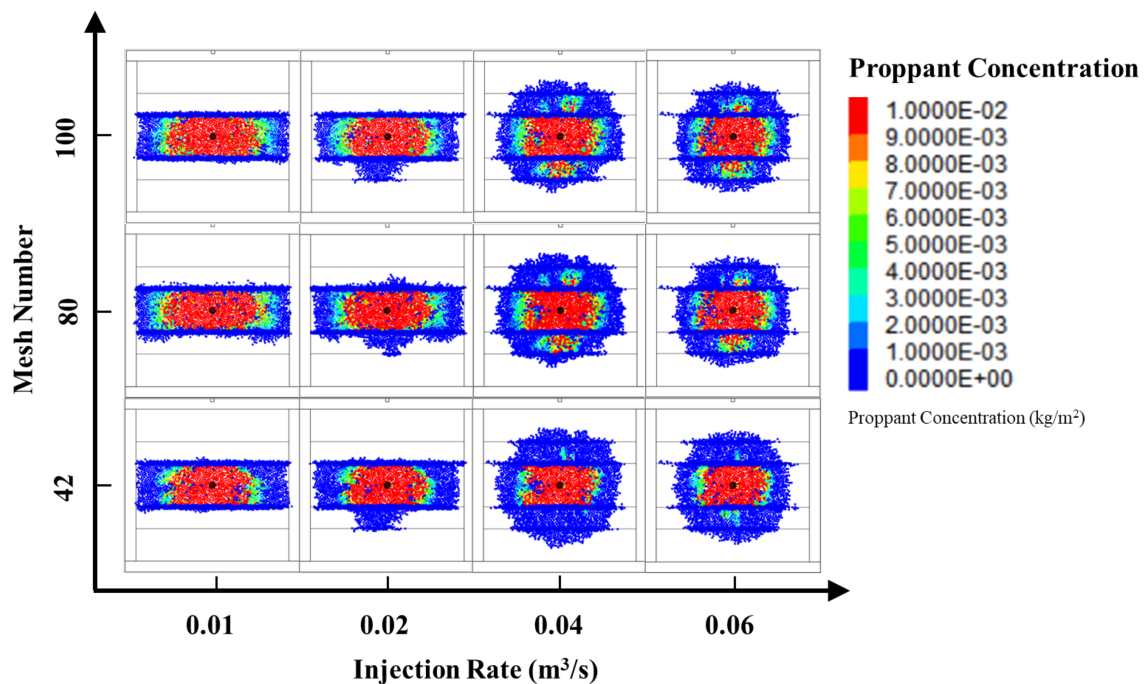
Figure 11. Variation of hydraulic fracture vertical propagation stimulated and propped area with fracturing fluid injection rate.

As seen from Figure 12, with the increase in injection rate, the stimulated area increases first and then decreases, and the maximum area appears at the injection rate of 0.04 m^3/s. This is because, with the increase in injection rate, the pressurization rate of the fluid in the fracture increases, which gives the fracture high energy to penetrate the upper and lower interlayers. However, when the injection rate is too high, a large amount of fracturing fluid flows into the reservoir quickly, which makes the fracture only increase the fracture width while being unable to propagate fully.
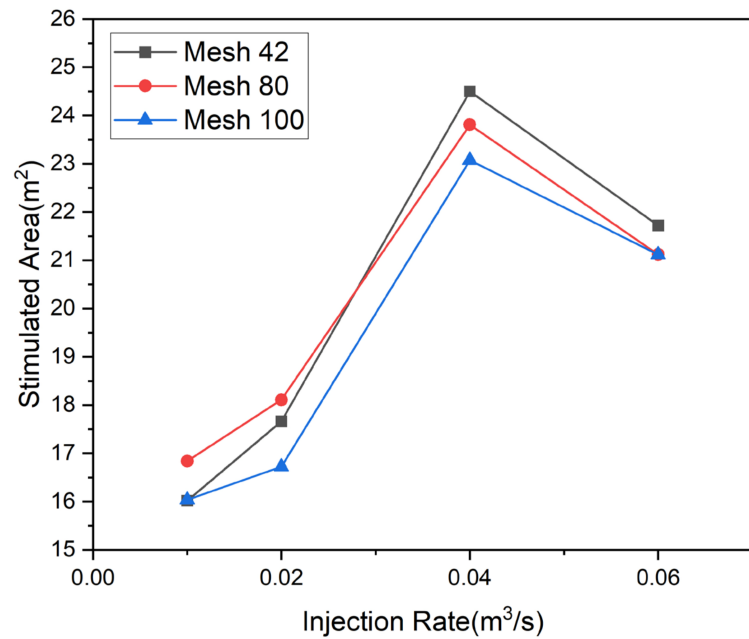
Figure 12. Effect of fracturing fluid injection rate on fracture stimulated area.

Furthermore, it can be seen from Figure 13 that, when the injection rate is 0.04 m^3/s, not only does the fracture obtain the maximum vertical stimulated area but it also obtains the relative maximum propped area, which is in line with our common perception that, the greater the stimulated area of the fracture, the greater the area propped by the proppant under the condition of a certain fracture width. However, when considering the influence of proppant size, it can be found that the area propped by coarse particle size proppant, such as 42 mesh, is much smaller than that of fine particle size proppant, which is because it is limited by the size factor, resulting in it being unable to transport into the relatively low fracture width area, limiting the transport distance of the proppant, presenting a relatively stable overall propped area, which is not affected by the injection rate. In contrast, the fine particle size proppant 80 and 100 mesh possess similar propped areas.
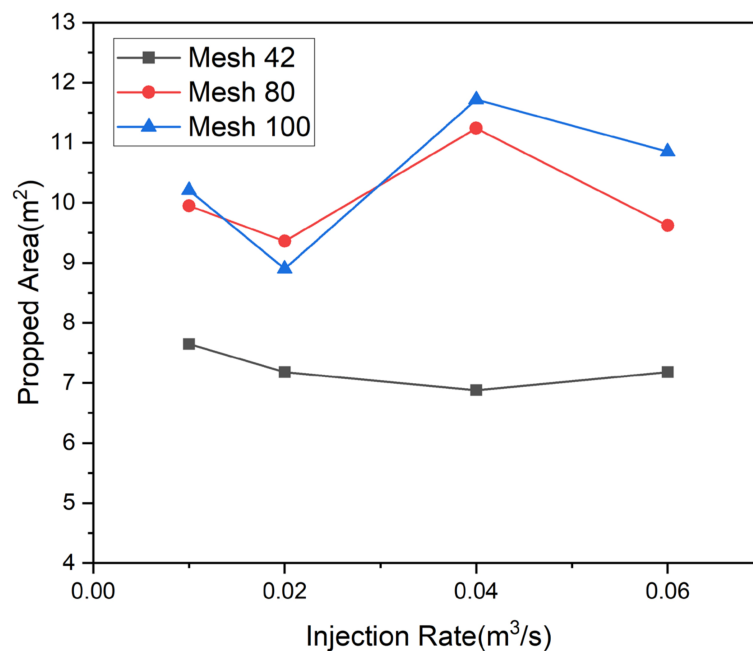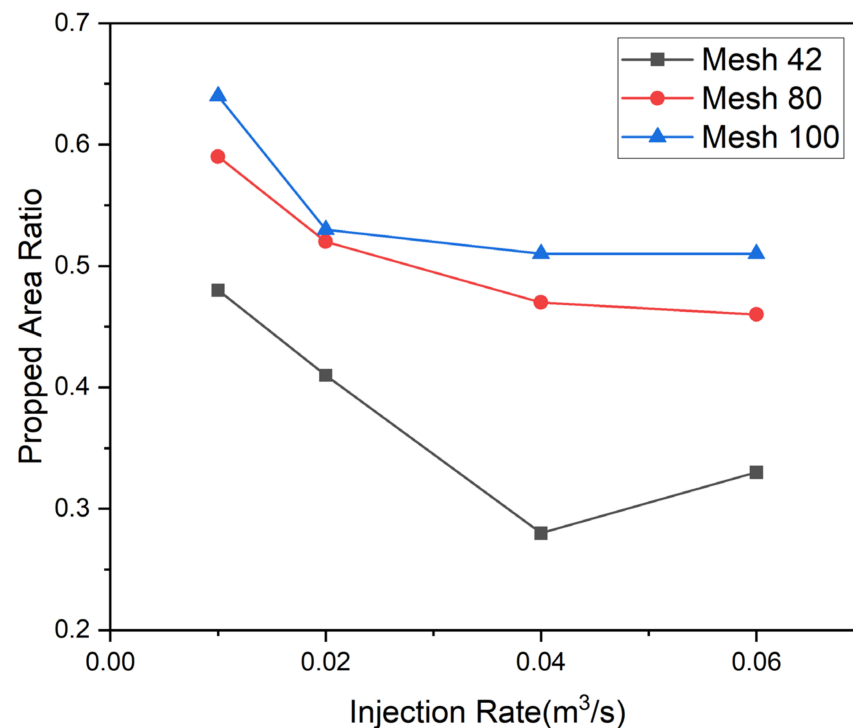

Figure 13. Effect of fracturing fluid injection rate on propped area.

As shown in Figure 14, the propped area ratio gradually decreases as the injection rate increases. From the figure, it is found that, when the injection rate is 0.01 and 0.02 m^3/s, the propped area ratio is greater and, the higher the injection rate, the smaller the propped area ratio, which is because when at a relatively low injection rate, it is difficult for the fracture to penetrate the layer interface and the main fracture only propagates in the pay layer. When the injection rate is 0.02 m^3/s, the fracture partially penetrates through the lower layer interface into the interlayer but there is no proppant in the interlayer fracture due to the barrier effect of the layer interface on the proppant, so the proportion of the propped area does not increase. In addition, when the injection rate is relatively high, i.e., from 0.04 to 0.06 m^3/s, the fracture propped area ratio hardly changes and, in these cases, the large particle size proppant is still blocked from entering the interlayer and the fracture propped ratio becomes higher as the particle size decreases.

Figure 14. Effect of fracturing fluid injection rate on propped area ratio.

In conclusion, with the increase in injection rate, it is easier for the hydraulic fracture to penetrate the interface to form a greater fracture area. Also, an ideal injection rate exists when the injection rate is too high; the fracture width increases significantly while the fracture area decreases slightly. Ultimately, it is found that the proppant had a greater impact on the propped area ratio.

5. Discussion

A 3D lattice-based fracture height propagation model was established. The geological formation was composed of five layers: three pay layers and two interlayers laid on each other. The variation law of fracture height growth was simulated and examined by varying formation stress and strength. The advantage of the 3D lattice-based fracture model over the KGD model is that it can consider the variation of fracture width at various heights. The variation of fracture width directly affects the proppant transport, which facilitates the study of proppant placement in fractures. Moreover, compared to other 3D fracture propagation simulation methods, the lattice-based method is capable of simulating the fracture height growth law under various lithological conditions.

In order to further analyze the hydraulic fracture height growth and proppant distribution law, changes in fracture propagation morphology were simulated under different formation conditions. The results reveal that Young's modulus, followed by the minimum principal stress, has the greatest influence on fracture morphology. In reality, Young's modulus of the adjacent layer usually does not differ considerably but the stress difference between the adjacent layer is substantial [46,47]. Therefore, the influence of stress anisotropy on fracture propagation morphology should be paid enough attention. The fracture height propagation under different operational parameters was analyzed. Increasing the fracturing fluid rate is a common production enhancement technique for unconventional reservoirs. By doing so, the stimulated volume can be increased.

There is a positive correlation between fracture propagation morphology and proppant distribution area. After it is clear that the fracture morphology rises in height, this paper focuses on the analysis of proppant distribution area in the fracture and the proportion of propped area to the total fracture area. Previous studies simply used the fracture area created by fracturing to represent the fracture effective stimulated area. However, due to the limitation of fracture width, proppant is unable to reach those fracture tips with small width, thus affecting the ultimate effective stimulation area. In this paper, after a thorough analysis of the influence of various parameters on fracture propagation area, the concept of propped area ratio is introduced. By analyzing the influence of various parameters on propped area ratio, the reservoir production can be effectively improved. Relevant lab experiments as well as an analytical model will be carried out to further verify the influence of parameters on fracture areas. Moreover, the method referred in this paper has a prospective application from the position of increasing oil recovery, especially in those fields where the majority of wells have already been subjected to primary hydraulic fracturing.

6. Conclusions

This paper conducted a study of the effect of various parameters in hydraulic fracturing operations on the mechanism of vertical propagation of hydraulic fractures in multi-layer reservoirs. For this purpose, a lattice-based hydraulic fracture propagation model was developed. Then, sensitivity analysis on fracturing fluid injection rate, interlayer rock mechanical parameters, and horizontal stress anisotropy was conducted.

When hydraulic fracture propagation is vertical in a multi-layer reservoir, the large interlayer Young's modulus, stress anisotropy, and injection rate are favorable to hydraulic fracture penetration into the upper and lower interlayer. The effect of injection rate on the fracture is two-sided. Both too low and too high injection rates inhibit fracture propagation; a 0.04 m^3/s injection rate has an optimal hydraulic fracture stimulated area.

In multi-layer reservoirs, as the fracture propagation area increases, the proppant propped area increases simultaneously. However, coarse particle size proppant provides less propped area compared to small particle size proppant, especially in interlayers; when fractures penetrate interlayers, coarse particle size proppant is relatively difficult to transport through the layer interface for propping due to its size limitation, while small particle size proppant can transport further into the fracture to prop. In addition, both the fracture stimulated area and propped area increase; the propped area ratio shows a decreasing trend. The selection of small particle size proppant can somewhat mitigate the effect of the reduced propped area ratio.

Author Contributions: Conceptualization, J.W.; investigation, G.P.; writing—original draft, J.W.; writing—review and editing, Z.C. and B.H. All authors have read and agreed to the published version of the manuscript.

Data Availability Statement: All the data required to evaluate the conclusions of this study are present in the paper. The authors will provide additional data related to this paper upon request.

Conflicts of Interest: The authors declare no conflict of interest.

References

1. Tang, J.; Wu, K.; Zuo, L.; Xiao, L.; Sun, S.; Ehlig–Economides, C. Investigation of Rupture and Slip Mechanisms of Hydraulic Fractures in Multiple-Layered Formations. *SPE J.* **2019**, *24*, 2292–2307. [CrossRef]
2. Xie, J.; Tang, J.; Yong, R.; Fan, Y.; Zuo, L.; Chen, X.; Li, Y. A 3-D hydraulic fracture propagation model applied for shale gas reservoirs with multiple bedding planes. *Eng. Fract. Mech.* **2020**, *228*, 106872. [CrossRef]
3. Li, Y.; Long, M.; Tang, J.; Chen, M.; Fu, X. A hydraulic fracture height mathematical model considering the influence of plastic region at fracture tip. *Pet. Explor. Dev.* **2020**, *47*, 184–195. [CrossRef]
4. Li, Y.; Long, M.; Zuo, L.; Li, W.; Zhao, W. Brittleness evaluation of coal based on statistical damage and energy evolution theory. *J. Pet. Sci. Eng.* **2018**, *172*, 753–763. [CrossRef]
5. Cong, Z.; Li, Y.; Pan, Y.; Liu, B.; Shi, Y.; Wei, J.; Li, W. Study on CO_2 foam fracturing model and fracture propagation simulation. *Energy* **2021**, *238*, 121778. [CrossRef]
6. Khristianovich, S.A.; Zheltov, V.P. Formation of vertical fractures by means of highly viscous liquid. In Proceedings of the 4th World Petroleum Congress, Rome, Italy, 6–15 June 2015; pp. 579–586.
7. Perkins, T.; Kern, L. Widths of Hydraulic Fractures. *J. Pet. Technol.* **1961**, *13*, 937–949. [CrossRef]
8. Geertsma, J.; De Klerk, F. A Rapid Method of Predicting Width and Extent of Hydraulically Induced Fractures. *J. Pet. Technol.* **1969**, *21*, 1571–1581. [CrossRef]
9. Nordgren, R.P. Propagation of a Vertical Hydraulic Fracture. *Soc. Pet. Eng. J.* **1972**, *12*, 306–314. [CrossRef]
10. Zhang, J.; Li, Y.; Pan, Y.; Wang, X.; Yan, M.; Shi, X.; Zhou, X.; Li, H. Experiments and analysis on the influence of multiple closed cemented natural fractures on hydraulic fracture propagation in a tight sandstone reservoir. *Eng. Geol.* **2021**, *281*, 105981. [CrossRef]
11. Li, Y.; Jia, D.; Rui, Z.; Peng, J.; Fu, C.; Zhang, J. Evaluation method of rock brittleness based on statistical constitutive relations for rock damage. *J. Pet. Sci. Eng.* **2017**, *153*, 123–132. [CrossRef]
12. Gravanis, E.; Sarris, E. A working model for estimating CO_2-induced uplift of cap rocks under different flow regimes in CO_2 sequestration. *Géoméch. Energy Environ.* **2023**, *33*, 100433. [CrossRef]
13. Isah, A.; Hiba, M.; Al-Azani, K.; Aljawad, M.S.; Mahmoud, M. A comprehensive review of proppant transport in fractured reservoirs: Experimental, numerical, and field aspects. *J. Nat. Gas Sci. Eng.* **2021**, *88*, 103832. [CrossRef]
14. Fetisov, V.; Ilyushin, Y.V.; Vasiliev, G.G.; Leonovich, I.A.; Müller, J.; Riazi, M.; Mohammadi, A.H. Development of the automated temperature control system of the main gas pipeline. *Sci. Rep.* **2023**, *13*, 3092. [CrossRef]
15. Bosikov, I.I.; Klyuev, R.V.; Mayer, V. Comprehensive assessment of hydraulic fracturing technology efficiency for well construction during hydrocarbon production. *J. Min. Inst.* **2022**, *258*, 1018–1025. [CrossRef]
16. Bosikov, I.I.; Martyushev, N.V.; Klyuev, R.V.; Savchenko, I.A.; Kukartsev, V.V.; Kukartsev, V.A.; Tynchenko, Y.A. Modeling and Complex Analysis of the Topology Parameters of Ventilation Networks When Ensuring Fire Safety While Developing Coal and Gas Deposits. *Fire* **2023**, *6*, 95. [CrossRef]
17. Cong, Z.; Li, Y.; Liu, Y.; Xiao, Y. A new method for calculating the direction of fracture propagation by stress numerical search based on the displacement discontinuity method. *Comput. Geotech.* **2021**, *140*, 104482. [CrossRef]
18. Wu, K.; Olson, J.E. Simultaneous Multifracture Treatments: Fully Coupled Fluid Flow and Fracture Mechanics for Horizontal Wells. *SPE J.* **2015**, *20*, 337–346. [CrossRef]
19. Zhu, W.; Shi, H.; Huang, B.; Zhong, K.; Huang, Y. Geology and geochemistry of large gas fields in the deepwater areas, continental margin basins of northern South China Sea. *Mar. Pet. Geol.* **2021**, *126*, 104901. [CrossRef]
20. Xue, D.; Zhou, J.; Liu, Y.; Gao, L. On the excavation-induced stress drop in damaged coal considering a coupled yield and failure criterion. *Int. J. Coal Sci. Technol.* **2020**, *7*, 58–67. [CrossRef]
21. Tian, Z.; Tang, C.; Liu, Y.; Tang, Y. Zonal disintegration test of deep tunnel under plane strain conditions. *Int. J. Coal Sci. Technol.* **2020**, *7*, 337–349. [CrossRef]
22. Hou, E.; Wen, Q.; Ye, Z.; Chen, W.; Wei, J. Height prediction of water-flowing fracture zone with a genetic-algorithm support-vector-machine method. *Int. J. Coal Sci. Technol.* **2020**, *7*, 740–751. [CrossRef]
23. Xue, J.; Wang, H.; Zhou, W.; Ren, B.; Duan, C.; Deng, D. Experimental research on overlying strata movement and fracture evolution in pillarless stress-relief mining. *Int. J. Coal Sci. Technol.* **2015**, *2*, 38–45. [CrossRef]
24. Zhao, X.; Jin, F.; Liu, X.; Zhang, Z.; Cong, Z.; Li, Z.; Tang, J. Numerical study of fracture dynamics in different shale fabric facies by integrating machine learning and 3-D lattice method: A case from Cangdong Sag, Bohai Bay basin, China. *J. Pet. Sci. Eng.* **2022**, *218*, 110861. [CrossRef]
25. Zhu, W.; Cui, Y.; Shao, L.; Qiao, P.; Yu, P.; Pei, J.; Liu, X.; Zhang, H. Reinterpretation of the northern South China Sea pre-Cenozoic basement and geodynamic implications of the South China continent: Constraints from combined geological and geophysical records. *Acta Oceanol. Sin.* **2021**, *40*, 13–28. [CrossRef]
26. Simonson, E.; Abou-Sayed, A.; Clifton, R. Containment of Massive Hydraulic Fractures. *Soc. Pet. Eng. J.* **1978**, *18*, 27–32. [CrossRef]
27. Ahmed, U. Fracture Height Prediction. *J. Pet. Technol.* **1988**, *40*, 813–815. [CrossRef]

28. Newberry, B.; Nelson, R.; Ahmed, U. Prediction of vertical hydraulic fracture migration using compressional and shear wave slowness. In *SPE/DOE Low Permeability Gas Reservoirs Symposium*; OnePetro: Richardson, TX, USA, 1985.

29. Economides, M.J. *Petroleum Production Systems*; Pearson Education: London, UK, 2013.

30. Li, Y.; Zhou, L.; Li, D.; Zhang, S.; Tian, F.; Xie, Z.; Liu, B. Shale Brittleness Index Based on the Energy Evolution Theory and Evaluation with Logging Data: A Case Study of the Guandong Block. *ACS Omega* **2020**, *5*, 13164–13175. [CrossRef]

31. Warpinski, N.R.; Mayerhofer, M.J.; Vincent, M.C.; Cipolla, C.L.; Lolon, E. Stimulating Unconventional Reservoirs: Maximizing Network Growth While Optimizing Fracture Conductivity. *J. Can. Pet. Technol.* **2009**, *48*, 39–51. [CrossRef]

32. Tong, S.Y.; Singh, R.; Mohanty, K.K. Proppant transport in fractures with foam-based fracturing fluids. In Proceedings of the SPE Annual Technical Conference and Exhibition, San Antonio, TX, USA, 9–11 October 2017; SPE-187376-MS. [CrossRef]

33. Katanov, Y.; Vaganov, Y.; Cheymetov, M. Neural simulation-based analysis of the well wall stability while productive seam penetrating. *Min. Miner. Depos.* **2021**, *15*, 91–98. [CrossRef]

34. Ma, Y.; Xu, Y. Research into technology for precision directional drilling of gas-drainage boreholes. *Min. Miner. Depos.* **2022**, *16*, 27–32. [CrossRef]

35. Tang, J.; Fan, B.; Xiao, L.; Tian, S.; Zhang, F.; Zhang, L.; Weitz, D. A New Ensemble Machine-Learning Framework for Searching Sweet Spots in Shale Reservoirs. *SPE J.* **2021**, *26*, 482–497. [CrossRef]

36. Keshavarz, A.; Badalyan, A.; Johnson, R.; Bedrikovetsky, P. Productivity enhancement by stimulation of natural fractures around a hydraulic fracture using micro-sized proppant placement. *J. Nat. Gas Sci. Eng.* **2016**, *33*, 1010–1024. [CrossRef]

37. Khanna, A.; Kotousov, A.; Sobey, J.; Weller, P. Conductivity of narrow fractures filled with a proppant monolayer. *J. Pet. Sci. Eng.* **2012**, *100*, 9–13. [CrossRef]

38. Damjanac, B.; Cundall, P. Application of distinct element methods to simulation of hydraulic fracturing in naturally fractured reservoirs. *Comput. Geotech.* **2016**, *71*, 283–294. [CrossRef]

39. Al-Tailji, W.H.; Shah, K.; Davidson, B.M. The application and misapplication of 100-mesh sand in multi-fractured horizontal wells in low-permeability reservoirs. In Proceedings of the SPE Hydraulic Fracturing Technology Conference, The Woodlands, TX, USA, 9–11 February 2016; SPE-179163-MS 2016.

40. Williams, R.; Artola, P.; Salinas, J.; Mirakyan, A.; MacKay, B.; Hoefer, A.; Kraemer, C.; Reese, H.; Roybal, Z.; Williamson, B. An early production comparison of northern white sand and regional sand in the Permian basin. In Proceedings of the SPE Annual Technical Conference and Exhibition, Calgary, AB, Canada, 30 September–2 October 2019; SPE-196048-MS 2019.

41. Patel, P.S.; Robart, C.J.; Ruegamer, M.; Yang, A. Analysis of US hydraulic fracturing fluid system and proppant trends. In Proceedings of the SPE Hydraulic Fracturing Technology Conference, The Woodlands, TX, USA, 4–6 February 2014; SPE 168645 2014.

42. Mohaghegh, S.D.; Gaskari, R.; Maysami, M. Shale analytics: Making production and operational decisions based on facts: A case study in Marcellus shale. In Proceedings of the SPE Hydraulic Fracturing Technology Conference and Exhibition, The Woodlands, TX, USA, 24–26 January 2017; SPE 184822 2017.

43. Yang, M.; Economides, M.J. Revisting natural proppants for hydraulic fracture production optimization. In Proceedings of the SPE Hydraulic Fracturing Technology Conference, The Woodlands, TX, USA, 6–8 February 2012; SPE 151934 2012.

44. Gu, H.; Siebrits, E. Effect of Formation Modulus Contrast on Hydraulic Fracture Height Containment. *SPE Prod. Oper.* **2008**, *23*, 170–176. [CrossRef]

45. Hanson, M.E.; Anderson, G.D.; Shaffer, R.J. Theoretical and Experimental Research on Hydraulic Fracturing. *J. Energy Resour. Technol.* **1980**, *102*, 92–98. [CrossRef]

46. Lei, T.; Yin, X.; Zong, Z. Pore pressure prediction in orthotropic medium based on rock physics modeling of shale gas. *J. Nat. Gas Sci. Eng.* **2020**, *74*, 103091. [CrossRef]

47. Zhang, J.; Xingyao, Y.; Zhang, G.; Yipeng, G.; Xianggang, F. Prediction method of physical parameters based on linearized rock physics inversion. *Pet. Explor. Dev.* **2020**, *47*, 59–67. [CrossRef]